RSC Advances

PAPER

View Article Online
View Journal | View Issue

Cite this: *RSC Adv.*, 2024, **14**, 36852

Characterization and enhanced carbon dioxide sensing performance of spin-coated Na- and Li-doped and Co-doped cobalt oxide thin films†

Rana Saad, ‡*[a] Khaled Abdelkarem, ‡*[ab] Adel M. El Sayed,[c] Mohamed Shaban,*[d] Inas A. Ahmed,[e] M. T. Tammam[a] and Hany Hamdy[a]

Received 22nd September 2024
Accepted 31st October 2024

DOI: 10.1039/d4ra06847e

rsc.li/rsc-advances

Recognizing the substantial effects of carbon dioxide on human health and the environment, monitoring CO_2 levels has become increasingly vital. Owing to energy constraints and the widespread application of CO_2 gas sensors, it is important to design cost-effective, more efficient, and faster response CO_2 gas sensors that operate at room temperature and involve a low-cost technique. This study aims to develop a cost-effective and efficient CO_2 gas detector that functions at room temperature and uses less power than traditional high-temperature CO_2 sensors. In this study, we achieved this by employing innovative Co_3O_4 thin films with optimized spinel-structured p-type semiconductors through spin-coating, facilitated by Li and Na doping as well as Li/Na codoping. Doping with 3% Li/Na reduced the crystallite size from 92.4 to 8.03 nm and increased the band gap from 3.31 to 3.69 eV. At room temperature (30 °C), the sensor response improved significantly, increasing from 50% to 345.01% for 3% Li-Co_3O_4 upon the addition of 3% Na at a concentration of 9990 ppm. This performance surpasses that of most metal-oxide-based CO_2 sensors reported in the literature. Additionally, this optimized sensor demonstrated a very short response time of 18.8 s and a recovery time of 16.4 s at a CO_2 concentration of 9990 ppm diluted with air. It outperformed other films in terms of sensitivity, stability, response and recovery times, and performance across a wide range of relative humidity levels (43–90%). The sensor exhibited superior selectivity for CO_2 than for N_2, H_2, and NH_3. Overall, the 3% Li, Na-Co_3O_4 sensor is well-suited for climate change mitigation and industrial applications.

1. Introduction

Increasing rates of greenhouse gas emissions and their associated greenhouse effect, which play a major role in warming Earth's atmosphere, are major issues in the global discussion on environmental safety.[1] Moreover, the world's population desires clean air with low levels of greenhouse gases (GHGs) such as ozone (O_3), fluorocarbons (F), methane (CH_4), nitrous oxide (N_2O), and carbon dioxide (CO_2).[2] Therefore, it is essential to detect the mentioned issues early to save human lives.[3] In this regard, gas sensors are essential for protecting the environment.[4,5] Gas sensors can monitor emissions from a range of sources, including transportation and industrial activities, to ensure that environmental regulations are followed and to lessen their impact on the ecosystem. CO_2 has begun to gain attention, which is not only a major GHG but also a vital sign of air quality, because increased levels of CO_2 may be harmful to human health and cause heating, ventilation and air conditioning (HVAC) system modifications. With the use of this information, organizations may reduce CO_2 emissions and support international efforts to combat climate change.[6] Several types of CO_2 gas sensors have been discussed in previous studies, such as infrared,[7] surface acoustic wave,[8] capacitive type,[9] solid electrolyte,[10] and resistive type[11–13] sensors. It has been shown that resistive gas sensors are great for detecting and measuring chemicals and gases because they have a direct electrical interface, respond quickly, and are very sensitive and cheap to fabricate.[14–16] Over the past few decades, a wide variety of resistive gas-sensing materials have been identified, such as conducting polymers,[17] conducting carbon nanomaterials,[18] and metal oxide semiconductors.[19,20] CO_2 sensors have been constructed with metal oxides such as ZnO,[21] WO_3,[22] CuO,[23]

---

[a] *Nanophotonics and Applications (NPA) Lab, Department of Physics, Faculty of Science, Beni-Suef University, Beni Suef 62511, Egypt. E-mail: ranasaad811@gmail.com; mtaha19@yahoo.com; hshamdy@hotmail.com*

[b] *Department of Physics, Chonnam National University, Gwangju 61186, Republic of Korea. E-mail: oldfighter.khaled123@gmail.com*

[c] *Department of Physics, Faculty of Science, Fayoum University, El-Fayoum 63514, Egypt. E-mail: ams06@fayoum.edu.eg*

[d] *Department of Physics, Faculty of Science, Islamic University of Madinah, P. O. Box: 170, Madinah 42351, Saudi Arabia. E-mail: mssfadel@aucegypt.edu*

[e] *Department of Chemistry, Faculty of Science, King Khalid University, Abha 62224, Saudi Arabia. E-mail: eaahmed@kku.edu.sa*

† Electronic supplementary information (ESI) available. See DOI: https://doi.org/10.1039/d4ra06847e

‡ Both authors equally contributed to this work.

In_2O_3,[24] TiO_2,[25] SnO_2,[26] Fe_2O_3,[27] and Co_3O_4.[28] They are frequently combined with metal ions, carbon compounds, or noble metals to improve their performance. Of these metal oxides, cobalt oxide exhibits catalytic activity in oxidation processes, making it a potential material for gas-sensing applications.[29] CoO and Co_3O_4 are the two primary forms of cobalt oxides. At RT and low relative pressures of oxygen, cobalt oxide is most thermally stable in its state as Co_3O_4. Co_3O_4 exhibits remarkable surface response and efficiently adsorbs gas molecules. When it interacts with target gases, the elevated surface response significantly alters its electrical characteristics, making it highly sensitive to a variety of gases including CO_2, CO, H_2S, and NH_3.[30] Also, Co_3O_4 can be synthesized as nanostructured films (nanoparticles, nanowires, or thin films), hence augmenting the surface-to-volume ratio. An increased surface area leads to a greater number of active sites for gas adsorption, thereby enhancing both sensitivity and response time.[31] In addition, the spinel structure of Co_3O_4 ($CoCo_2O_4$) is AB_2O_4, with Co^{2+} ions occupying the tetrahedral sites and Co^{3+} ions occupying the octahedral sites.[32] Previously published literature used cobalt oxide to detect CO_2 gas; for example, D. Y. Kim *et al.* used cobalt oxide mixed with barium carbonate to improve the sensor response of pure Co_3O_4 at 150 °C and 10 000 ppm CO_2 gas concentration, which reached a 30% sensor response.[33] G. Joshi *et al.* improved the sensor response of Co_3O_4 at RT and 500 mg L^{-1} CO_2 gas concentration with SnO_2, which reached 13.68%.[34] L. Gómez *et al.* used Eu- and La-based cobaltites to improve the sensor response of perovskite cobaltites $LnBaCo_2O_{5+\delta}$. Depending on the different amounts of oxygen on the surfaces of cobaltite compounds, a 4% sensor response was observed at 300 °C and 400 ppm CO_2 gas concentration.[35] Based on these previous studies,[31–33] there is a need to develop more efficient and cost-effective Co_3O_4-based CO_2 sensors operating at room temperature to meet industrial requirements. In busy industrial environments, continuous machinery operation can lead to unexpected CO_2 leaks from cylinders or production lines, as well as incidents like malfunctioning of HVAC systems or accidental CO_2 releases. Therefore, this study aims to design a low-cost and efficient CO_2 gas sensor that operates at room temperature and consumes less power than conventional high-temperature CO_2 sensors.[36] This study focuses on developing more efficient CO_2 gas sensors at concentrations higher than 1000 ppm using innovative and cost-effective Co_3O_4 thin films. By optimizing spinel-structured p-type semiconductor Co_3O_4 thin films through spin-coating, we enhance their performance with Li and Na doping, as well as Li/Na codoping. This doping and codoping usually raise the band gap of Co_3O_4. This alteration increases the sensor's responsiveness to gas adsorption and improves its capacity to detect gases at lower concentrations. An expanded band gap facilitates the observation of resistance variations during gas interactions, hence enhancing the overall detection capability.[37] The study examines the improved electrical and optical properties, morphology, and surface structure of the doped and co-doped Co_3O_4 sensors using various analytical tools. Additionally, the dynamic response is analyzed and the sensing performance indicators are correlated.

2. Experimental work

2.1. Fabrication of thin films

The preparation process of the thin films is illustrated in Fig. 1(a). Pure and doped 0.06 M solutions were made by dissolving cobalt acetate tetrahydrate ($(CH_3COO)_2Co\cdot 4H_2O$, 249.08 g mol^{-1}, Merck) in 7 ml of ethanol. The solution was heated at 50 °C with magnetic stirring for two hours. After 10 minutes of stirring, a few drops of acetic acid were added to the solution to obtain a clear and homogeneous solution. After another 10 minutes of stirring the mixture, a few drops of polyvinylpyrrolidone (PVP) solution as a chelating agent were added. For doping with 3% Li and 3% Na, we added to the solution 0.0005 g and 0.001 g of lithium chloride (LiCl, 42.394 g mol^{-1}, Merck) and sodium chloride (NaCl, 58.44 g mol^{-1}, Merck), respectively. The same ratios were added for codoping with 3% Li and 3% Na. Then, all solutions were aged for 24 hours at RT. Before forming thin films, the cleaning process of the glass substrates was done with the utmost care. This is because the cleaning step is very important to get a smooth film without pinholes that hold well to the material. First, the glass substrates were washed in a soap solution and then cleaned with deionized water. After that, they were immersed in ethanol and then deionized water. At the end, an N_2 gun was used to dry the glass substrates. Spin coating was done at a speed of 2000 rpm for a total of 25 s, with each layer being heated to 200 ° C. The coating and drying process was repeated several times to obtain films with the desired thickness. The last step was to put all of the thin films in an air furnace at 500 °C for two hours.

2.2. Thin film characterization

Various techniques were used for analyzing the prepared thin films. A scanning electron microscope was used to study the thin film morphology (SEM Auriga Zeiss FIB, ZEISS Microscopy, Munich, Germany). In addition, the SEM apparatus includes a unit for performing energy-dispersive X-ray analysis (EDX; Oxford Link ISIS 300, Concord, MA, USA). X-ray diffraction (XRD) was carried out with a high-resolution PANalytical X′ Pert Pro MPD at a scanning speed of 0.02° min^{-1} across the entire 2θ range of 10–80°, using CuK_α radiation with a wavelength of 0.15406 nm. Fourier transform infrared spectroscopy (FTIR, Shimadzu, Kyoto, Japan) was performed to detect the functional groups with the spectrophotometer model number Shimadzu FTIR-340 Jasco. For optical studies, a double-beam spectrophotometer (PerkinElmer, Lamba 990 UV/Vis/NIR, PerkinElmer Inc., Waltham, MA, USA) was utilized.

2.3. Gas sensing measurements

Fig. 1(b) shows the standard commercial metal oxide gas sensing measurement system. It has a 1.0 L three-neck round-bottom flask with rubber O-rings at the top of its necks separating into the gas inlet, gas outlet, and an electrical signal. A 100% CO_2 gas cylinder (supplied by the Beni-Suef Factory for medical and industrial gases) with synthetic air in the flask was used, and the gas flow was controlled with an Alicat MC-500SCCM-D gas mass flow controller (Hethel, Norwich, UK).

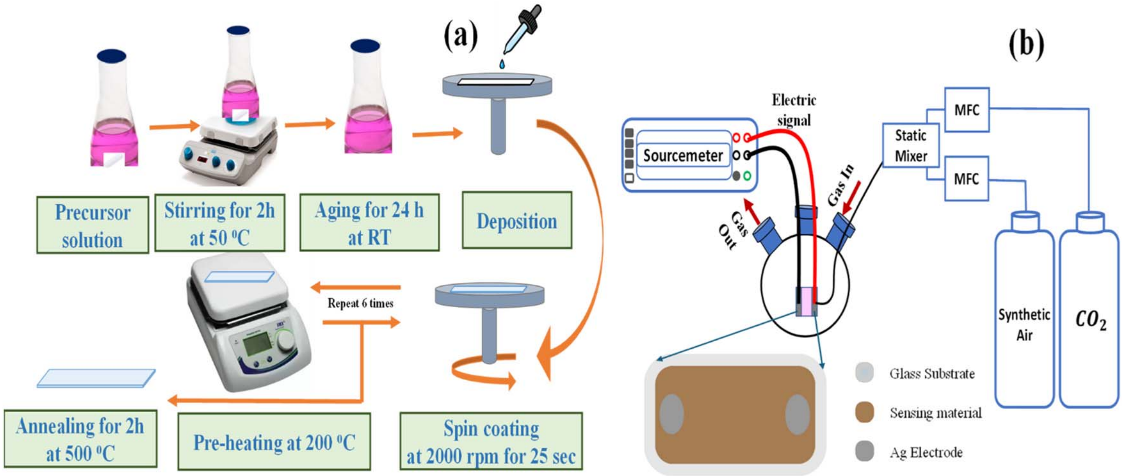

Fig. 1 The schematic of (a) spin-coating technique for the preparation of the thin films and (b) apparatus used for gas sensing measurement.

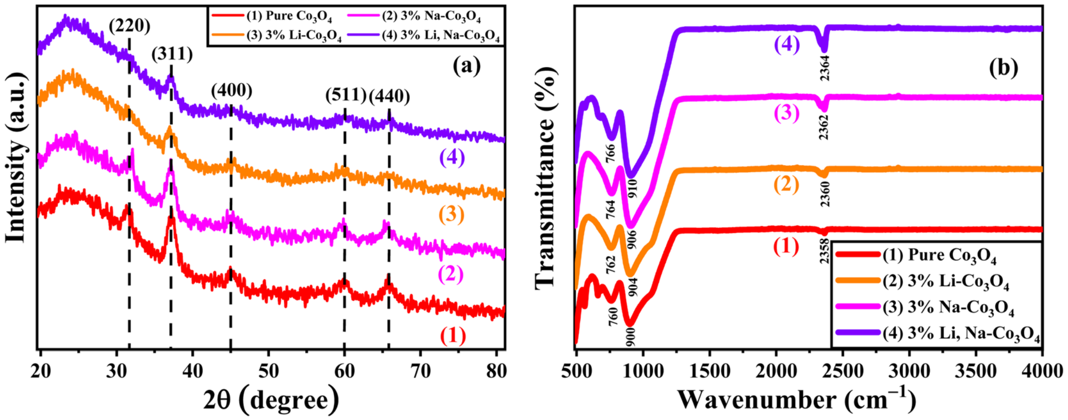

Fig. 2 (a) XRD and (b) FTIR spectra of pure Co_3O_4, 3% Li-Co_3O_4, 3% Na-Co_3O_4, and 3% Li, Na-Co_3O_4 thin films.

An extremely thin layer of Ag was added on both ends of the thin film to gather charges before it was connected *via* copper wires to the Keithley source measure device (model 2450, Tektronix, Beaverton, OR, USA). During data collection, the experimental equipment was kept at room temperature (RT, 30 °C) and relative humidity (RH, 43%). The sensor voltages were analyzed at varying CO_2 concentrations: 1110, 3330, 5550, 7770, and 9990 ppm. The repeatability and stability of the 3% Li, Na-Co_3O_4 thin film were measured at 9990 ppm, RT and 43% RH. For the selectivity test at 9990 ppm, we used excellent-quality (99.999%) cylinders (supplied by the Beni-Suef Factory for medical and industrial gases) of CO_2, nitrogen (N_2), hydrogen (H_2), and ammonia (NH_3) gases with synthetic air, and controlled the gas concentration with an Alicat MC-500SCCM-D gas mass flow controller (Hethel, Norwich, UK).

3. Results and discussion

3.1. XRD analysis

Fig. 2(a) shows the XRD spectra of pure Co_3O_4, 3% Li-Co_3O_4, 3% Na-Co_3O_4, and 3% Li, Na-Co_3O_4 thin films, which indicate the polycrystalline nature of these thin films. From the provided reference code 01-80-1542, the peaks at 2θ positions of 31.39°, 37.27°, and 45.00° relate to the diffraction planes (220), (311), and (400) of Co_3O_4 with the cubic spinel crystal structure, respectively. The mentioned structure belongs to the $Fd\bar{3}m$ space group. The presence of peaks corresponding to Co_3O_4 in the data indicates the absence of contaminants arising from Li or Na. The observed shifts in peak positions upon doping with Li^+ and Na^+ can be explained by the disparity in ionic radii among Co^{3+} (0.67 Å), Co^{2+} (0.74 Å), Li^+ (0.60 nm), and Na^+ (0.102 nm).[38,39] The observed considerable difference in peak values is attributed to the ability of Li^+ and Na^+ ions to replace Co^{3+} and Co^{2+} ions inside the crystal lattice of Co_3O_4.[40] Using XRD data, the crystallite size was estimated by the Debye–Scherrer eqn (1) and is recorded in Table 1:

$$D = \frac{k\lambda}{\beta \cos \theta} \tag{1}$$

where 'k' is the shape factor ($k = 0.9$), λ is the wavelength of X-rays, β is the full-width at half maximum (FWHM), and (θ) is the angle of incident radiation (in degrees). The crystallite size

Table 1 XRD parameters of pure Co_3O_4, 3% Li-Co_3O_4, 3% Na-Co_3O_4, and 3% Li, Na-Co_3O_4 thin films

Parameters samples	ε ($\times10^{-3}$)	δ ($\times10^{15}$ m^{-2})	d311 (Å)	a (Å)	FWHM β311 (°)	D (nm)
Pure Co_3O_4	19.4	0.117	2.417	8.01	0.090	92.4
3% Li-Co_3O_4	11.2	0.12	2.45	8.13	0.090	91.1
3% Na-Co_3O_4	13.7	5.42	2.41	7.99	0.614	13.58
3% Li, Na-Co_3O_4	24.05	15.51	2.40	7.95	0.998	8.03

values are reduced upon doping with 3% Li, and 3% Na, and the reduction of crystallite size increases upon codoping with 3% Li and Na, as shown in Table 1. For measuring lattice parameters, we use eqn (2):

$$d^2 = \frac{a^2}{h^2 + l^2 + k^2} \tag{2}$$

The variable d denotes the distance between lattice points, a refers to the lattice parameter, and the symbols h, k, and l are used to indicate Miller indices. The microstrain (ε) of the prepared Co_3O_4 thin films was evaluated using the following eqn (3):

$$\varepsilon = \frac{\beta \cos \theta}{4} \tag{3}$$

The length of dislocation lines per unit volume of the crystal is known as the dislocation density (δ), calculated using eqn (4):

$$\delta = \frac{1}{D^2} \tag{4}$$

3.2. FTIR analysis

Fourier transform infrared spectroscopy (FTIR) was used to determine the chemical structure of the functional groups present on the surface of pure Co_3O_4, 3% Li-Co_3O_4, 3% Na-Co_3O_4, and 3% Li, Na-Co_3O_4 thin films, as shown in Fig. 2(b).[41,42] Two peaks around 760 cm^{-1} and 900 cm^{-1} appeared due to the stretching vibration modes associated with Co^{2+}–O and Co^{3+}–O, respectively. These peaks originate from the spinel structure of Co_3O_4, specifically the tetrahedral and octahedral regions.[43] The asymmetric vibration (C═O) of CO_2 taken from the air during the thermal treatment of metal oxides is shown by peaks at around 2358 cm^{-1}.[44,45] As seen in Fig. 2(b), the CO_2 peaks were at 2358, 2360, 2362, and 2364 cm^{-1} for pure Co_3O_4, 3% Li-Co_3O_4, 3% Na-Co_3O_4, and 3% Li, Na-Co_3O_4 thin films, respectively. The doping and co-doping lead to a shift towards higher wavenumbers and an increase in intensity. The increasing intensity of this peak indicates that the interaction between CO_2 and the thin film surface is developing as intended.[46,47]

3.3. UV-vis spectroscopy analysis

UV-vis spectroscopy was used to measure the optical absorption spectra and band gap of pure Co_3O_4, 3% Li-Co_3O_4, 3% Na-Co_3O_4, and 3% Li, Na-Co_3O_4 thin films. Fig. 2(a) shows the optical absorption spectra of the produced thin. These spectra show two absorption peaks in the UV and visible regions.[48] These peaks appear at 409 nm and 752 nm, 407 nm and 748 nm, 405 nm and 738 nm, and 400 nm and 736 nm for pure Co_3O_4, 3% Li-Co_3O_4, 3% Na-Co_3O_4, and 3% Li, Na-Co_3O_4, respectively. The shift towards shorter wavelengths (blue shift) indicates an increase in the band gaps, as seen in Fig. 3(b) and recorded in Table 2. The nature and value of the optical band gap are determined by the fundamental absorption, which corresponds to the electron excitation from the valence band to the conduction band.[49,50] The Tauc plot was used to calculate the band gap, based on eqn (5), which describes the relationship between absorption coefficients (α) and incident photon energy ($E = h\nu$).[51]

$$(\alpha h\nu)^2 = A(E - E_g) \tag{5}$$

where h is the Planck constant, which is equal to 6.626×10^{-34} $m^2\ kg\ s^{-1}$, E_g is the band gap energy, and A is a constant number that doesn't depend on the frequency of the photon.

The E_g values were obtained by extrapolating the linear portions of $(\alpha h\nu)^2$ *vs.* $h\nu$ curves to zero absorption. As shown in Table 2, the band gap increases with 3% Li and 3% Na doping and with 3% Li, Na co-doping.[52] Fig. 3(c) shows the electrical band structure of cobalt oxide, contributing to the existence of two band gaps in this material. While the $O_2 \rightarrow Co^{3+}$ charge transfer is related to the lower band gap (E_{g1}) because the Co^{3+} level is placed below the conduction band, the $O_2 \rightarrow Co^{2+}$ charge transfer process is associated with the larger band gap (E_{g2}).[53,54] Although E_{g2} is the true band gap in Co_3O_4, this dual-band gap nature is reported for other materials.[55]

3.4. SEM, surface roughness, and EDX analysis

Scanning electron microscopy (SEM) was used to determine the morphology of the Co_3O_4 thin films, as it is the most common technique for obtaining the nanostructural and surface characteristics of prepared thin films.[56,57] All films exhibit a similar morphology. There are a large number of particles per unit area, and the substrates are well covered by the Co_3O_4 material. As shown in Fig. 4(a), the SEM image of pure Co_3O_4 reveals a large number of tiny quite homogeneous cracks distributed throughout the film surface.[58] After doping with Li, as shown in Fig. 4(b), Co_3O_4 nanoparticles agglomerate and comprise a smaller grain size.[59] In addition, Fig. 4(c) shows that doping with Na promotes crack formation, where the crack widens and appears with larger lengths. Because the nucleation energy barrier has decreased, there are more nucleation sites, which may explain why the surface distribution of 3% Li-Co_3O_4 and 3% Na-Co_3O_4 thin films is better.[60] Following co-doping with 3% Na and 3% Li, plenty of cracks are formed, as depicted in

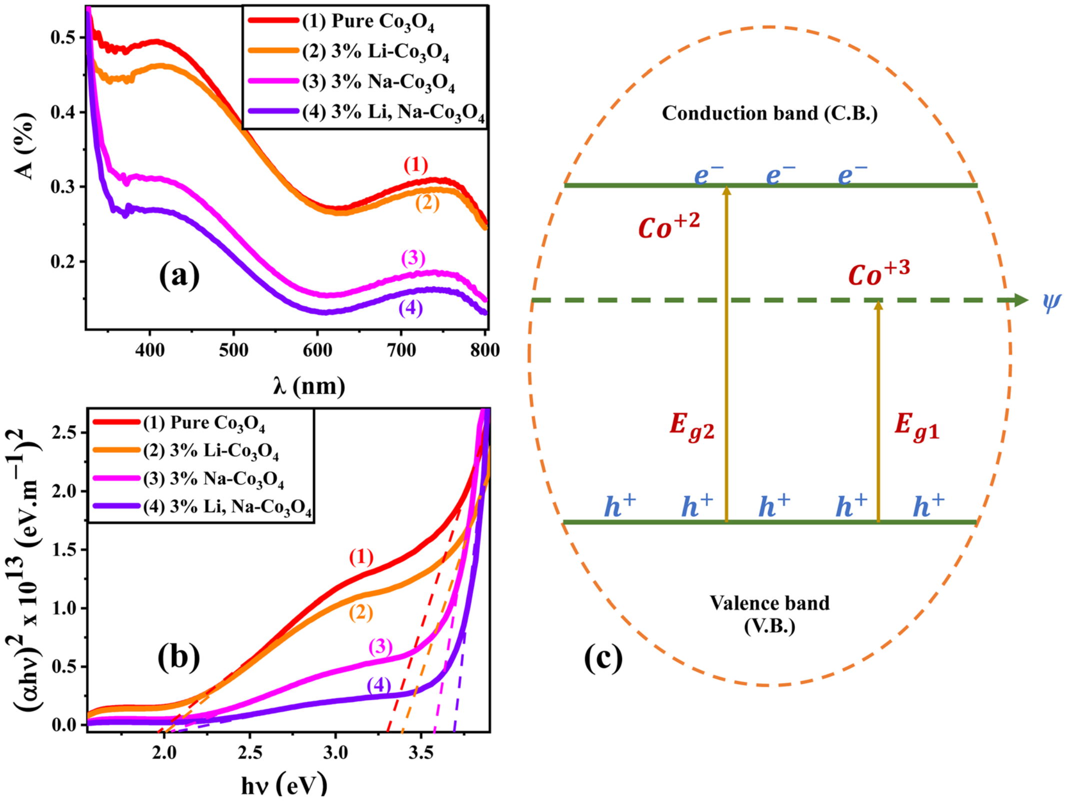

Fig. 3 (a) Absorption spectrum and (b) band gap energy plots of pure Co_3O_4, 3% Li-Co_3O_4, 3% Na-Co_3O_4, and 3% Li, Na-Co_3O_4 thin films, and (c) the band structure of Co_3O_4.

Table 2 The band gaps (E_{g1} and E_{g2}) of pure Co_3O_4, 3% Li-Co_3O_4, 3% Na-Co_3O_4, and 3% Li, Na-Co_3O_4

Thin film	E_{g1} (eV)	E_{g2} (eV)
Pure Co_3O_4	1.96	3.31
3% Li-Co_3O_4	2.01	3.39
3% Na-Co_3O_4	2.05	3.58
3% Li, Na-Co_3O_4	2.09	3.69

Fig. 4(d), increasing the exposed area to the gas and enhancing gas detection capability and sensitivity. ImageJ was used to evaluate the roughness of the surfaces of pure Co_3O_4, 3% Li-Co_3O_4, 3% Na-Co_3O_4, and 3% Li, Na-Co_3O_4, shown in Fig. 4(e–h). The surface roughness of the 3% Li-Co_3O_4 and 3% Na-Co_3O_4 thin films is higher than that of pure Co_3O_4 (Fig. 4(f) and (g)) because there are more cracks due to doping. Along with cracks, the nucleation rate is higher in 3% Li, Na-Co_3O_4 (Fig. 4(h)), causing the surface to be rougher. As a result, the surface area and the response of the 3% Li, Na-Co_3O_4 thin films to gases is higher.[61] Gwyddion software showed that the root-mean-square roughness (R_{rms}) of Co_3O_4 thin films was 1.84 for pure Co_3O_4, 2.03 for 3% Li-Co_3O_4, and 2.55 for 3% Na-Co_3O_4. In contrast, the RMS roughness increased to 3.21 nm for 3% Li, Na-Co_3O_4. According to the earlier work, the surface area can also be increased by making the 3% Li, Na-Co_3O_4 surface rougher. The reason is that the 3% Li, Na-Co_3O_4 has a higher roughness level, which means that it covers more surface area than the other thin films. This means that the response of the 3% Li, Na-Co_3O_4 sensor for gases is better than those of other Co_3O_4 thin films.[62] The homogeneous distributions of cobalt (Co), oxygen (O), sodium (Na), and lithium (Li) in 3% Li, Na-Co_3O_4 thin film nanoparticles were identified using EDX elemental mapping shown in Fig. 4(i–l).

EDX analysis was used to determine the nanomaterial's chemical purity and stoichiometry.[63] Fig. 5(a–d) depicts the EDX spectra of the prepared pure Co_3O_4, 3% Li-Co_3O_4, 3% Na-Co_3O_4, and 3% Li, Na-Co_3O_4, respectively. The obtained result verified the presence of a homogeneous distribution of Li^+ and Na^+ ions within the Co_3O_4 system. The peaks that appeared at around 0.8, 7.0, and 7.6 keV were related to the Co element, while oxygen (O) was found to have a peak at 0.5 keV. Unfortunately, because Li has a low atomic number, it can't be detected with EDX, and there were no peaks related to it as previously reported.[64–66] According to the EDX spectrum, the peak at 1.04 keV confirms the presence of the Na element.[67]

3.5. Current–voltage characteristics and dynamic response

Fig. 6(a–d) shows the current–voltage (*I*–*V*) characteristics of the gas sensors over a voltage range of 0 to 10 V when the sensors were exposed to synthetic air and a 5550 ppm concentration of CO_2 at room temperature. The *I*–*V* curves depict the ideal ohmic behavior of the sensors. Because the sensitivity of the gas sensor is influenced by contact resistance, ohmic behavior is a very

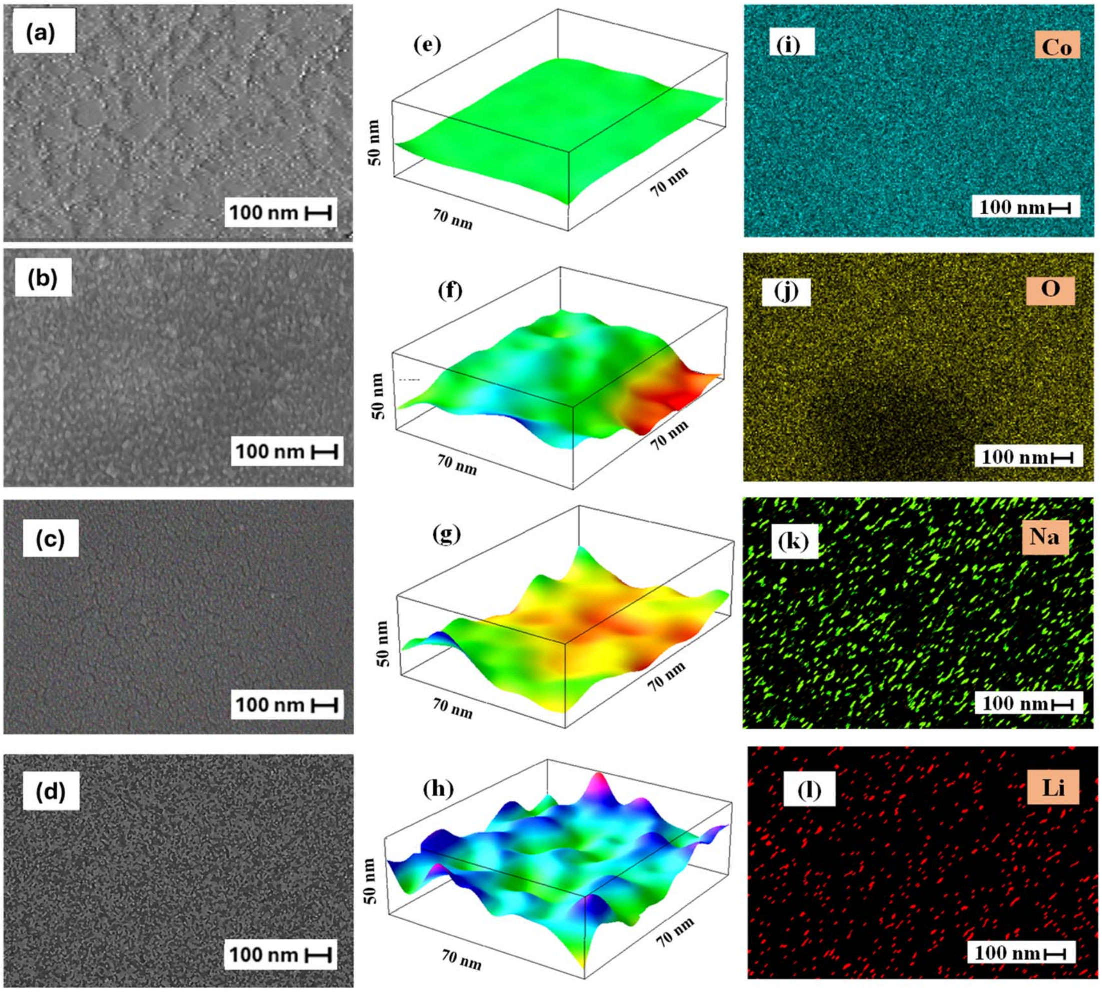

Fig. 4 SEM images for Co_3O_4 thin films: (a) pure Co_3O_4, (b) 3% Li-Co_3O_4, (c) 3% Na-Co_3O_4, and (d) 3% Li, Na-Co_3O_4. Surface roughness for Co_3O_4 thin films: (e) pure Co_3O_4, (f) 3% Li-Co_3O_4, (g) 3% Na-Co_3O_4, and (h) 3% Li, Na-Co_3O_4. (i–l) EDX elemental mapping of 3% Li, Na-Co_3O_4.

important aspect of gas sensing.[68–70] As shown in Fig. 6(a–d), the presence of CO_2 increased the electrical resistance from 0.0049 to 0.0051 GΩ, 0.34 to 0.4 GΩ, 0.27 to 0.33 GΩ, and 1.61 to 12.21 GΩ for pure Co_3O_4, 3% Li-Co_3O_4, 3% Na-Co_3O_4, and 3% Li, Na-Co_3O_4, respectively. Pure Co_3O_4 has a low sensitivity, almost negligible, to CO_2, while the responses of 3% Li-Co_3O_4 and 3% Na-Co_3O_4 to CO_2 become obvious. The CO_2 response is further enhanced in the case of 3% Li, Na-Co_3O_4, as seen in Fig. 4(d). This confirms the gradient shown by the FTIR in the interaction with CO_2, where the 3% Li, Na-Co_3O_4 thin film surface showed the highest interaction with CO_2. During this study, the Co_3O_4 thin films were exposed to various concentrations of CO_2 gas (1110, 3330, 5550, 7770, and 9990 ppm) balanced with air at room temperature. Subsequently, the sensing parameters were determined through an analysis of these figures. The observed behaviors can be explained by the adsorption and desorption processes occurring on the film's surface, which involve the interaction between CO_2 molecules and adsorbed oxygen. Depending on the nature of CO_2, a non-polar gas, the resistance of the sensor increases until it reaches a stable state. When the supply of CO_2 gas is stopped and air is brought into the chamber system, the resistance of the sensor drops quickly until it reaches its initial resistance. Fig. 6(e–g) shows that doping with 3% Li and 3% Na, and co-doping with 3% Li, Na make the sensor response better at a 9990 ppm gas concentration; the resistance is much higher for 3% Li, Na-Co_3O_4 than for 3% Na-Co_3O_4 and 3% Li-Co_3O_4. So, the 3% Li, Na-Co_3O_4 thin film is the best CO_2 sensor compared to the 3% Na-Co_3O_4 and 3% Li-Co_3O_4 thin films.

3.6. Sensor response, concentration sensitivity, and response and recovery times

According to the dynamic response in Fig. 6(e–g), the sensor response (R%) can be calculated using eqn (6) (ref. 71) and the result recorded in Fig. 7(a).

$$R\% = \left|\frac{R_{CO_2} - R_{air}}{R_{air}}\right| \times 100 \tag{6}$$

where R_{CO_2} and R_{air} are the measured resistances in CO_2 and air environments, respectively. The value of R_{CO_2} is calculated from the dynamic response after a certain exposure time to CO_2, and the value of R_{air} is measured under the same conditions.[72,73] As

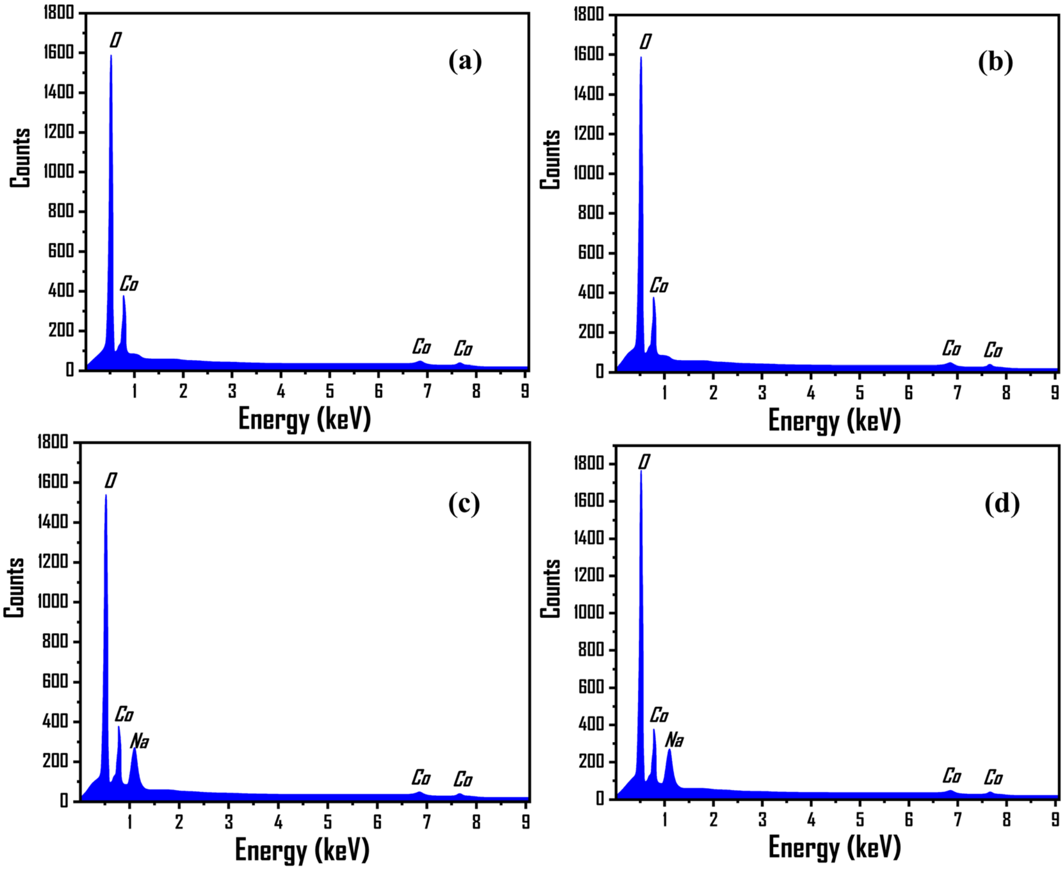

Fig. 5 EDX spectra for Co_3O_4 thin films: (a) pure Co_3O_4, (b) 3% Li-Co_3O_4, (c) 3% Na- Co_3O_4, and (d) 3% Li, Na-Co_3O_4.

shown in Fig. 6, as the gas concentration increased, the sensitivity and gas response of the Co_3O_4 thin film also increased as it was doped with 3% Li and 3% Na and codoped with 3% Li, Na. Specifically, the values remained low for the reaction of 3% Na-Co_3O_4 and 3% Li-Co_3O_4 in Fig. 7(a). As the concentration increased from 1110 ppm to 9990 ppm, the sensor response

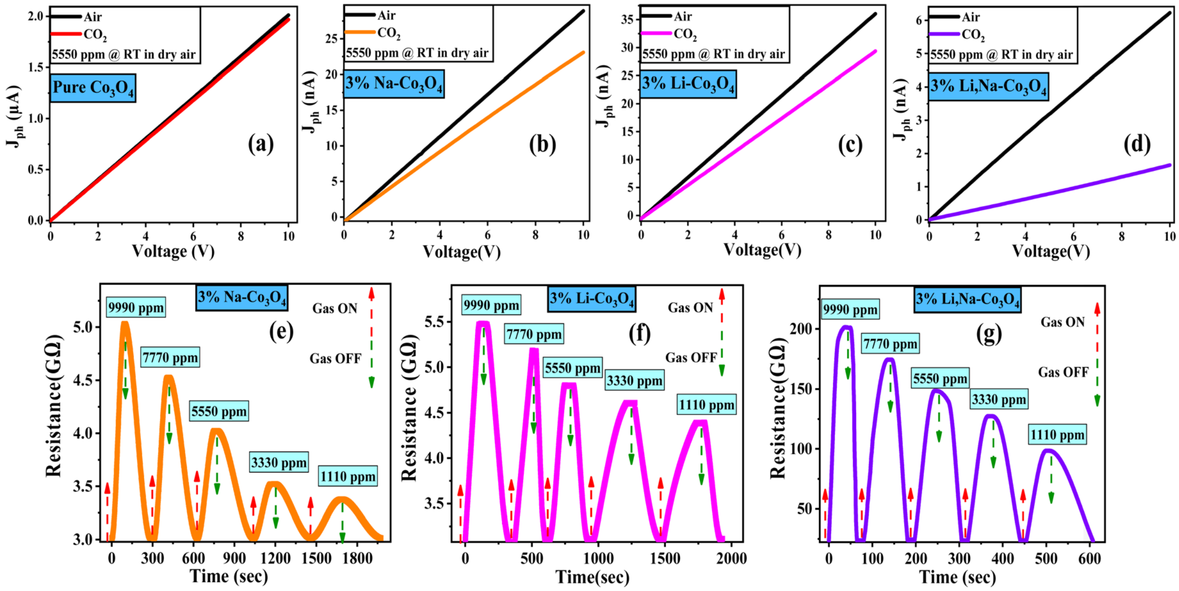

Fig. 6 Current–voltage (*I*–*V*) curves of (a) pure Co_3O_4, (b) 3% Li-Co_3O_4, (c) 3% Na-Co_3O_4, and (d) 3% Li, Na-Co_3O_4 thin films. Dynamic response of (e) 3% Li-Co_3O_4, (f) 3% Na-Co_3O_4, and (g) 3% Li, Na-Co_3O_4 thin films, and (h) the sensor response *versus* concentration.

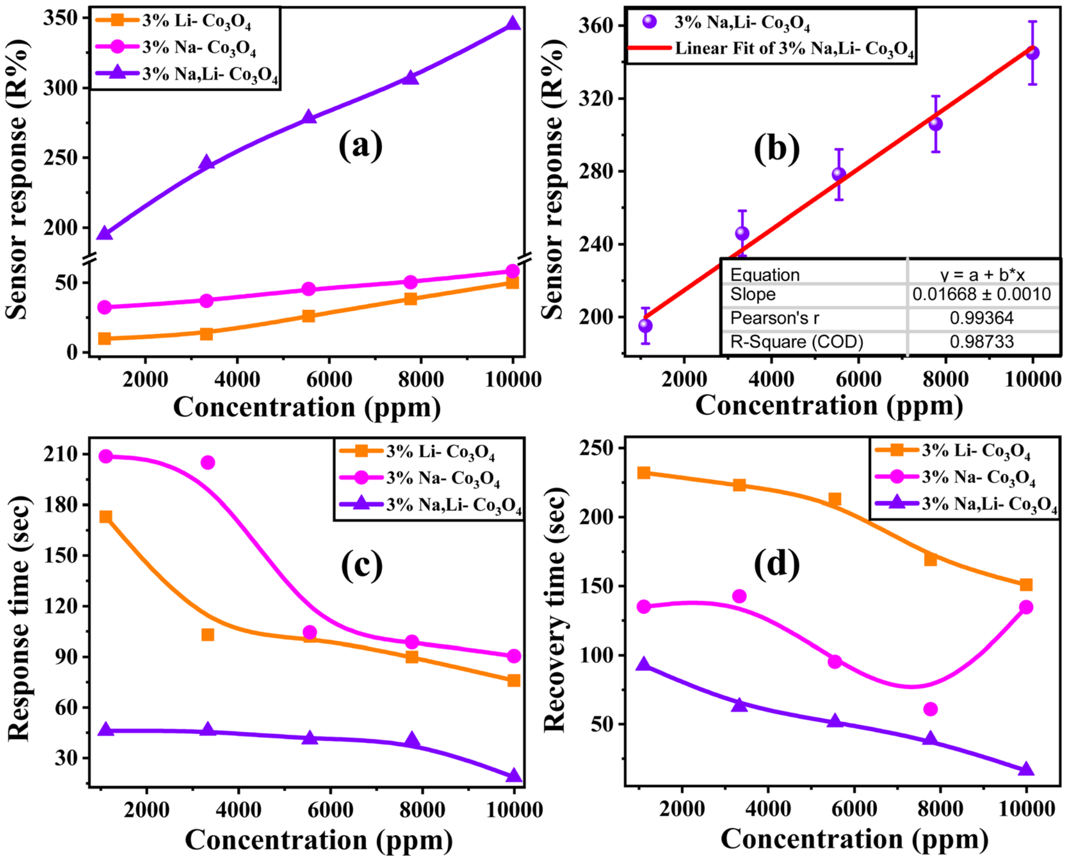

Fig. 7 (a) The sensor response of 3% Li-Co_3O_4, 3% Na-Co_3O_4, and 3% Li, Na-Co_3O_4 thin films. (b) Linear fitted sensor response *versus* CO_2 concentration, (c) the response time, and (d) the recovery time of all Co_3O_4 thin films *vs.* different gas concentrations at RT and 43% RH.

increased from 9.86% to 50% for 3% Li-Co_3O_4, whereas for 3% Na-Co_3O_4, it increased from 32.3% to 58.3%. On the other hand, the response values for 3% Li, Na-Co_3O_4 demonstrated an enormous improvement, rising from 195.1% to 345.01%. This enhancement is due to the increased sensitivity and surface roughness.[74,75] As illustrated in Fig. 7, the 3% Li, Na-Co_3O_4 sensor exhibited the most significant surface roughness, which led to its superior ability to respond to CO_2 gas. Additionally, it shows rapid response and recovery times. As shown in Fig. 7(b), for the linearly fitted sensor response *vs.* CO_2 concentration graph, the slope (concentration sensitivity) was computed to be 0.01668 ppm^{-1}. The practical value of this linear relationship extends to gas-sensing devices.[76] The relation between the gas concentration and the estimated response time of the Co_3O_4 sensors is illustrated in Fig. 7(c). The response time is the amount of time necessary for the change in relative resistance to reach a point at 90% of its value adhering to exposure to CO_2. In addition, Fig. 7(d) shows the recovery time, indicating the period required to acquire a resistance that is 10% greater than its initial value.[77] At a concentration of 9990 ppm, the response times of 3% Li-Co_3O_4 and 3% Na-Co_3O_4 were 76 and 90.5 s, respectively, whereas 3% Li, Na-Co_3O_4 exhibited a response time of 18.8 s. In the same way, the recovery times at a similar concentration were 151 s and 92.6 s for 3% Li-Co_3O_4 and 3% Na-Co_3O_4, respectively, and 16.4 s for 3% Li, Na-Co_3O_4. Based on the data gathered it can be concluded that codoping caused a decrease in both the response and recovery times. The noticed improvement is a result of the raised surface roughness of the film. Surface roughness increases due to the formation of cracks, which provide additional adsorption sites for gas molecules.[78] When CO_2 molecules come into contact with the rough surface, they can chemisorb onto the active sites (such as oxygen vacancies or defect sites).[79] Also, CO_2 molecules can easily penetrate the crack structure, allowing for efficient interaction with the sensor,[80] which has a beneficial impact on the film's response to and recovery from CO_2 gas.[81]

3.7. Repeatability, and long-term stability

The repeatability of sensor responses is important for practical application. Fig. 8(a) shows high repeatability for the 3% Li, Na-Co_3O_4 sensor's response, which nearly remains constant after exposure to CO_2 for 10 cycles at RT and 43% RH. Fig. 8(b) shows the 3% Li, Na-Co_3O_4 sensor's long-term stability for 30 days. It maintains a sensor response of around 345.01% despite daily exposure to 9990 ppm CO_2 at RT and 43% RH. This demonstrated that the sensor was reliable and able to be used for a long time. Overall, the results showed that the 3% Li, Na-Co_3O_4 sensor is highly stable and repeatable when exposed to CO_2 gas.

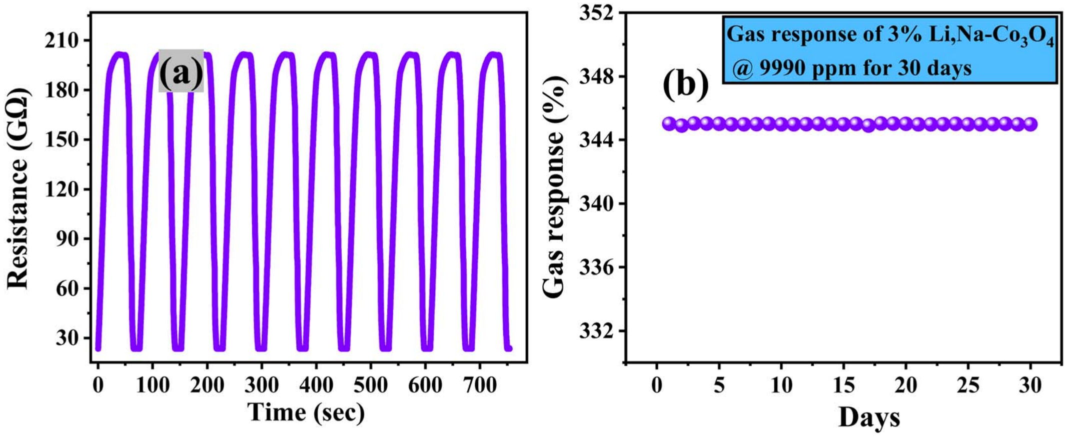

Fig. 8 (a) Repeatability and (b) stability of 3% Li, Na-Co_3O_4 thin films at RT and 43% RH.

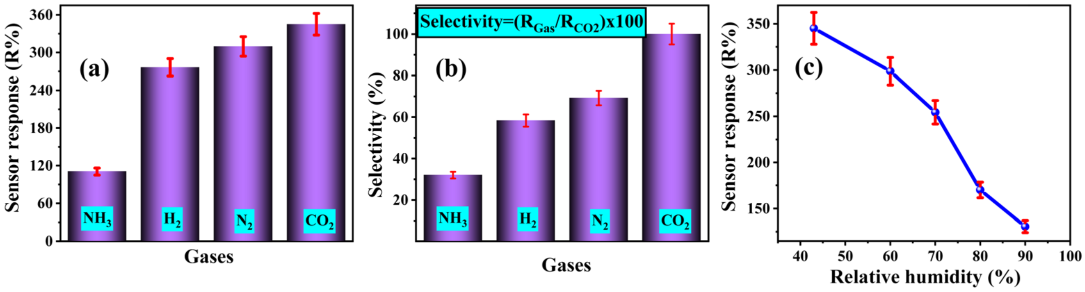

Fig. 9 (a) The sensor response and (b) selectivity of the 3% Li, Na-Co_3O_4 sensor for several gases at 9990 ppm concentration, RT and 43% RH, and (c) sensor response under various relative humidity levels at RT.

3.8. CO_2 selectivity and relative humidity effect

A significant area of concern for metal oxide-based gas sensors is selectivity. So selectivity is one of the most important factors to take into consideration while assessing the features of gas sensors. The selectivity of a sensor is determined by testing the device with a range of gases and calculating the sensor response ratio for each gas using eqn (7).

$$\text{Selectivity}(\eta\%) = \frac{R_{\text{other gas}}}{R_{\text{target gas}}} \times 100 \tag{7}$$

To investigate the selectivity of the 3% Li, Na-Co_3O_4 sensor, we expose it to various gases such as N_2, H_2, and NH_3. We then analyze the sensor's dynamic response, calculate the sensor's response for each gas, and finally calculate the ratio of the sensor's response to the target gas, CO_2. According to Fig. 9(a), the 3% Li, Na-Co_3O_4 sensor was the most sensitive to CO_2 compared to all the gases that were tested ($R_{CO_2} > R_{N_2} > R_{H_2} > R_{NH_3}$). Fig. 9(b) shows the selectivity for different gases along with CO_2, with the percentages for N_2, H_2, and NH_3 being 69.25%, 58.4%, and 32.05%, respectively.

To study the impact of humidity, the sensing test of the 3% Li, Na-Co_3O_4 sensor was carried out under relative humidity levels ranging from 43% to 90%. It emerged that the gas response decreased with relative humidity, as seen in Fig. 9(c). There have also been many studies reporting an identical influence of humidity on gas detection.[82,83] Surface-sensitive Co_3O_4 sites were decreased by the reaction with water molecules.[84] Consequently, 3% Li, Na-Co_3O_4 showed low gas reactivity to CO_2 as the humidity increased. Therefore, significant work needs to be done in the future to lessen the impact of humidity on the sensing capabilities of 3% Li, Na-Co_3O_4 sensors.

3.9. Sensor detection and quantification limits, and signal to noise ratio

The limit of detection (DL) of the sensor was calculated using the standard deviation (SD) and the slope of the figure depicting sensor response percentage relative to gas concentration, Fig. 7(a), using eqn (8).[85]

$$\text{DL} = \frac{3 \times \text{SD}}{\text{slope}} \tag{8}$$

The DL for 3% Li-Co_3O_4 was 2.899 ppm as the slope was 0.00475 ppm^{-1} and the SD was 0.00459, but for 3% Na-Co_3O_4 the DL was determined to be 1.83 ppm as the slope was 0.01621 ppm^{-1} and the SD was 0.00989. On the other hand, with great performance, the detection limit for 3% Li, Na-Co_3O_4 was determined to be 1.638 ppm, as the slope was 0.00295 ppm^{-1} and the SD was 0.00161.

Table 3 Comparison of CO_2 gas detection from earlier research investigations utilizing nanostructured semiconductor metal oxide sensors and the current work

Sensor	Operating temperature (°C)	Concentration (ppm)	Sensor response (R%)	References
Co_3O_4	150	10 000 ppm	30	33
SnO_2-Co_3O_4	RT	500 ppm	13.68	34
$LnBaCo_2O_{5+\delta}$	300	400 ppm	4	35
ZnO/CNTs	RT	16 650 ppm	22.4	72
Ba-CuO	RT	11 100 ppm	9.4	73
ZnO: 4.0 at% La	RT	22 200 ppm	114.22	75
p-Si/MoO_3	250	100 ppm	12.08	88
GO	RT	50 ppm	29	89
$BaTiO_3$-CuO	300	5000 ppm	9	90
Au-La_2O_3/SnO_2	300	100 ppm	10.1	91
Pure SnO_2	RT	—	78.57	92
CuO/ZnO (C/Z)	375	2500 ppm	47	93
3% Li, Na-Co_3O_4	RT	9990 ppm	345.01	This work

Also, we have determined the sensor's limit of quantification (QL), which refers to the minimum number of CO_2 molecules that the sensor can detect and can be measured using eqn (9).[86]

$$\mathrm{QL} = \frac{10 \times \mathrm{SD}}{\mathrm{slope}} \tag{9}$$

The QL for 3% Li-Co_3O_4 was 9.66 ppm, while the QL for 3% Na-Co_3O_4 was determined to be 6.101 ppm. However, the QL for 3% Li, Na-Co_3O_4 was determined to be 5.46 ppm. The DL and QL results indicate that the 3% Li, Na-Co_3O_4 film is the most effective one since it has the lowest detection and quantification limits.

The signal-to-noise ratio (S/N) was determined by applying eqn (10), involving the peak height (H) at the lowest concentration and the full width at half maximum (FWHM) (h).[87]

$$\frac{\mathrm{S}}{\mathrm{N}} = \frac{2H}{h} \tag{10}$$

The S/N for 3% Li-Co_3O_4 was 2 as the h was 7 cm and the H was 7.01 cm, but for 3% Na-Co_3O_4, the S/N was determined to be 2.54 as the h was 10 cm and the H was 12.53 cm, while the S/N for 3% Li, Na-Co_3O_4 was determined to be 1.85 as the h was 12.4 cm and the H was 11.51 cm.

The results obtained for DL, QL, and S/N show that the sensor with 3% Li, Na-Co_3O_4 is the most effective, as indicated by its better results, possessing the lowest detection and quantification limits in addition to the lowest signal-to-noise ratio. Moreover, Table 3 compares the data of previous research on sensors used for CO_2 gas, confirming the enhanced sensing abilities of our improved sensor.[33–35,72,73,75,88–93]

3.10. Gas sensing and relative humidity effect mechanism

The change in electrical resistance of the sensing material plays an important role in the chemiresistive gas sensing process of metal oxide semiconductors (MOX). When gases react with the surface of MOX, charge carriers move between the gas and MOX. This changes the electrical conductance based on the type of majority carriers of MOX and the type of gas the MOX is exposed to (oxidizing or reducing). When reducing gases react with p-type semiconductors, sensor resistance increases.[94]

Doping with Li and Na shifts the band gap of the Co_3O_4 thin film from 1.96 to 2.09 eV, thereby decreasing the inherent carrier concentration.[95] The enlarged band gap increases the sensor's sensitivity by intensifying the impact of gas adsorption on the surface. Because there are fewer free carriers, the baseline conductivity goes down. This makes the sensor more sensitive to changes in surface charge, which makes gas response easier.[96] Furthermore, co-doping induces defects, including oxygen vacancies, which significantly influence the material's electrical conductivity. These defects increase the number of active sites for gas adsorption, subsequently changing conductivity. When gas molecules interact with these active sites, they change the resistance of the thin film and the way charges move through it. This results in an observable sensing response.[97] This is clearly confirmed from Fig. 6, where the sensor's resistance increased from 0.0049 to 1.61 GΩ in air and from 0.0051 to 12.21 GΩ in a CO_2 environment with the codoping of 3% Li and Na.

When Co_3O_4 as a p-type semiconductor is exposed to air, oxygen is adsorbed at the surface. The oxygen molecules capture free electrons from the conduction band of Co_3O_4 and form ionized oxygen species (O^-, O_2^-, and O_2^-) depending on the operating temperature as shown in eqn (11)–(13), resulting in a positively charged surface leading to an increased hole accumulation layer thickness, which results in decreased resistance of Co_3O_4, depicted in Fig. 10(b).[98]

$$O_{2(\mathrm{ads})} + e^- \rightarrow O_{2(\mathrm{ads})}^- \text{ for temperature } <100\ ^\circ\mathrm{C} \tag{11}$$

$$O_{2(\mathrm{ads})}^- + e^- \rightarrow 2O_{(\mathrm{ads})}^- \text{ for a temperature range of } 100\text{–}300\ ^\circ\mathrm{C} \tag{12}$$

$$O_{(\mathrm{ads})}^- + e^- \rightarrow O_{(\mathrm{ads})}^{2-} \text{ for temperatures higher than } 300\ ^\circ\mathrm{C} \tag{13}$$

As shown in Fig. 6(e–g), the resistance quickly increased after the interaction between CO_2 and the Co_3O_4 sensor, which was

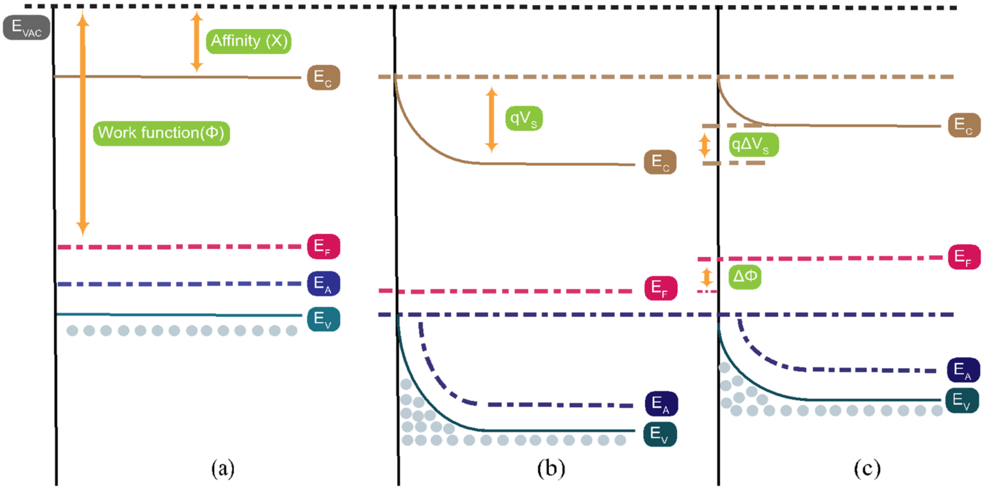

Fig. 10 The energy band structure of the Co_3O_4 surface (a) before any reaction, (b) when exposed to oxygen, and (c) when CO_2 gas is injected into the chamber. The term "E_C" denotes the location of the conduction band, "E_F" denotes the location of the Fermi level, "E_V" denotes the location of the valence band, "q" denotes the charge of the electron, and "qV_S" denotes the potential barrier.

attributed to an adsorption/desorption mechanism of CO_2 on the surface of the Co_3O_4 sensor. When CO_2 gas enters the chamber, it gets adsorbed onto the Co_3O_4 sensor's surface. This CO_2 then reacts with ionized oxygen species present on the surface, as illustrated in eqn (14) and (15). This reaction releases free electrons back to the sensor surface, where they recombine with holes, leading to a reduction in the hole accumulation layer (HAL) thickness. Consequently, this increases the resistance of the Co_3O_4 sensor, as shown in Fig. 10(c).[99]

$$CO_{2(gas)} \rightarrow CO_{2(ads)} \tag{14}$$

$$CO_{2(ads)} + O_{2(ads)}{}^{-} \rightarrow CO_{(gas)} + 2O_{2(gas)} + 2e^{-} \tag{15}$$

After the CO_3O_4 sensor reacts with oxygen molecules and forms oxygen species at room temperature, H_2 gas is injected into the chamber. H_2 gas reacts with oxygen species, and the produced free electrons recombine with holes, as described by eqn (16) and (17):

$$H_2 + O_{(ads)}{}^{-} \rightarrow e^{-} + H_2O \tag{16}$$

$$H_2 + O_{(ads)}{}^{2-} \rightarrow 2e^{-} + H_2O \tag{17}$$

As a result of this process, the concentration of holes and the thickness of the HAL decrease, leading to an increase in sensor resistance.[100]

When the CO_3O_4 sensor encounters NH_3 gas, NH_3 reacts with oxygen species as shown in eqn (18), which produces N_2, H_2O, and free electrons, and these electrons migrate back to the sensor's surface, causing an increase in resistance due to electron–hole recombination.[101]

$$4NH_3 + 3O_{(ads)}{}^{2}– \rightarrow 2N_2 + 6H_2O + 3e^{-} \tag{18}$$

when the Co_3O_4 sensor encounters N_2 gas, N_2 interacts with the oxygen species adsorbed on the sensor's surface, resulting in the formation of NO and the release of free electrons, as depicted in eqn (19). These free electrons migrate to the sensor's surface, leading to a reduction in the hole accumulation layer (HAL) thickness and an increase in the sensor's resistance.[102]

$$N_2 + 2O_{(ads)}{}^{-} \rightarrow 2e^{-} + 2NO \tag{19}$$

Owing to humidity in gas sensing mechanisms, water molecules (H_2O) split into hydroxyl ions (OH^-) and protons (H^+) when they interact with the metal-oxide surface. The adsorbed H_2O influences the active sites of the adsorption mechanism. At low humidity levels, H_2O ions chemisorb at the active sites of the CO_3O_4 surface, forming OH^- and H^+. These hydroxyl ions react with oxygen and form root hydroxyl groups; on the other hand, protons react with oxygen and form secondary hydroxyl ions (OH^+).[103] At high humidity levels, water molecules interact with gas molecules, which decreases the amount of adsorbed oxygen species and gas molecules.[104]

4. Conclusion

The spin-coating approach effectively generated thin films of 3% Li-Co_3O_4, 3% Na-Co_3O_4, and 3% Li, Na-Co_3O_4 at lower temperatures. We utilized XRD, SEM, EDX, FTIR, and UV-vis optical absorption spectroscopy techniques to investigate the impact of doping and codoping on the surface morphology, phase purity, and band gap energy of the thin films. The prepared Co_3O_4 thin films were used as CO_2 sensors at RT. The sensor response increased from 50% for 3% Li-Co_3O_4 and 58.3% for 3% Na-Co_3O_4 to 345.01% for 3% Li, Na-Co_3O_4 for a 9990 ppm concentration at RT and RH, which is higher than those of most metal-oxide-based sensors. By codoping with 3% Li and 3% Na, the response and recovery times of the Co_3O_4 sensor were significantly reduced to 18.8 s and 16.4 s, respectively. The 3% Li, Na-Co_3O_4 sensor exhibited excellent responsiveness with a detection limit of 1.638 ppm, a quantification limit of 5.46 ppm, and a signal-to-noise ratio of 1.85. The sensor operated efficiently at a relative humidity of 43% and an ambient temperature of 30 °C. Additionally, this sensor exhibited superior selectivity for CO_2 over gases like N_2, H_2, and NH_3. Overall, our research demonstrates that 3% Li, Na-Co_3O_4 thin films have superior sensor response and selectivity as CO_2 gas sensors, giving an attractive option for real-time indoor air quality monitoring at RT and therefore helping the global effort to combat climate change. While our study demonstrates effective CO_2 sensing, practical applications have some limitations. Further testing under diverse environmental conditions is necessary to validate sensor robustness. Ensuring long-term stability and durability is crucial, as continuous operation may lead to degradation. Additionally, the precise control required for thin film fabrication may pose challenges for large-scale manufacturing. Developing scalable techniques and exploring cost-reduction strategies are essential for broader adoption.

Data availability

The data presented in this study are available on request from the corresponding author.

Author contributions

Conceptualization, R. S., K. A., A. M. E., M. T. T. and M. S.; methodology, R. S., A. M. E., and M. S.; validation, R. S., K. A., A. M. E., M. T. T., M. S., and H. H.; formal analysis, R. S., K. A., A. M. E., M. T. T. and M. S.; investigation, R. S., K. A., A. M. E., M. T. T., M. S., and H. H.; resources, R. S., A. M. A., H. H., and M. S.; data curation, R. S., A. M. E., and M. S.; writing—original draft preparation, R. S., K. A., and M. S.; writing—review and editing, R. S., K. A., A. M. E., M. T. T. and M. S.; visualization, R. S., K. A., A. M. E., M. T. T., M. S., and H. H.; project administration, R. A., M. S., M. T. T., and H. H.; funding acquisition, R. A., and M. S. All authors have read and agreed to the published version of the manuscript.

Conflicts of interest

The authors declare no competing interests associated with this research.

Acknowledgements

This work was assisted financially by the Dean of Science and Research at King Khalid University *via* the General Research Project (grant number. RGP2(128/45). The authors extend their appreciation to the Deanship of Scientific Research at King Khalid University for funding this work through large group Research Project under grant number) RGP2(128/45).

References

1 United States Environmental Protection Agency, Climate Change Indicators: Greenhouse Gases, *Clim. Chang. Indic.*, 2023, pp. 1–12, Online. Available: **https://www.epa.gov/climate-indicators/greenhouse-gases**.

2 Y. K. Gautam, K. Sharma, S. Tyagi, A. K. Ambedkar, M. Chaudhary and B. Pal Singh, Nanostructured metal oxide semiconductor-based sensors for greenhouse gas detection: Progress and challenges, *R. Soc. Open Sci.*, 2021, **8**(3), DOI: **10.1098/rsos.201324**.

3 H. Zhang, *et al.*, PDMS Film-Based Flexible Pressure Sensor Array with Surface Protruding Structure for Human Motion Detection and Wrist Posture Recognition, *ACS Appl. Mater. Interfaces*, 2024, **16**(2), 2554–2563, DOI: **10.1021/ACSAMI.3C14036/SUPPL_FILE/AM3C14036_SI_001.PDF**.

4 N. Analysis, A. Intelligenceautomotiveembeddedindustrialiotmcumedicalmemory, S. A. Managementquantumstartupssoctest, C. S. Paperteardownhow-to, C. Directory, and P. Magazinesebooks, *Protecting the Climate with Gas Sensors*, 2022, pp. 1–9.

5 H. Zhang, D. Zhang, B. Zhang, D. Wang and M. Tang, Wearable Pressure Sensor Array with Layer-by-Layer Assembled MXene Nanosheets/Ag Nanoflowers for Motion Monitoring and Human-Machine Interfaces, *ACS Appl. Mater. Interfaces*, 2022, **14**(43), 48907–48916, DOI: **10.1021/ACSAMI.2C14863/SUPPL_FILE/AM2C14863_SI_006.MP4**.

6 S. A. Vanalakar, M. G. Gang, V. L. Patil, T. D. Dongale, P. S. Patil and J. H. Kim, Enhanced Gas-Sensing Response of Zinc Oxide Nanorods Synthesized via Hydrothermal Route for Nitrogen Dioxide Gas, *J. Electron. Mater.*, 2019, **48**(1), 589–595, DOI: **10.1007/S11664-018-6752-1/METRICS**.

7 Y. Li, *et al.*, Development and field deployment of a mid-infrared CO and CO2 dual-gas sensor system for early fire detection and location, *Spectrochim. Acta, Part A*, 2022, **270**, 120834, DOI: **10.1016/j.saa.2021.120834**.

8 C. Wang, *et al.*, Surface acoustic wave sensor based on Au/TiO2/PEDOT with dual response to carbon dioxide and humidity, *Anal. Chim. Acta*, 2022, **1190**, 339264, DOI: **10.1016/j.aca.2021.339264**.

9 C. Hagleitner, *et al.*, Smart single-chip gas sensor microsystem, *Nature*, 2001, **414**(6861), 293–296, DOI: **10.1038/35104535**.

10 S. Tamura and N. Imanaka, Solid electrolyte-type gas sensors applied trivalent cation conducting solid electrolytes, *Sens. Actuators, B*, 2022, **368**, 132252, DOI: **10.1016/j.snb.2022.132252**.

11 A. K. Singh, N. K. Chowdhury, S. C. Roy and B. Bhowmik, Review of Thin Film Transistor Gas Sensors: Comparison with Resistive and Capacitive Sensors, *J. Electron. Mater.*, 2022, **51**(5), 1974–2003, DOI: **10.1007/s11664-022-09485-y**.

12 N. N. Prabhu, R. B. Jagadeesh Chandra, B. V. Rajendra, G. George, A. H. I. Mourad and B. Shivamurthy, Electrospun Zinc Oxide Nanofiber Based Resistive Gas/Vapor Sensors - A Review, *Eng. Sci.*, 2022, **19**, 59–82, DOI: **10.30919/es8d612**.

13 X. Kang, N. Deng, Z. Yan, Y. Pan, W. Sun and Y. Zhang, Resistive-type VOCs and pollution gases sensor based on SnO2: A review, *Mater. Sci. Semicond. Process.*, 2022, **138**(2021), 106246, DOI: **10.1016/j.mssp.2021.106246**.

14 X. Qiao, Mo doped BiVO4 gas sensor with high sensitivity and selectivity towards H2S, *Chem. Eng. J.*, 2020, **395**, 125144, DOI: **10.1016/j.cej.2020.125144**.

15 A. Husain, S. Ahmad and F. Mohammad, Synthesis, characterisation and ethanol sensing application of polythiophene/graphene nanocomposite, *Mater. Chem. Phys.*, 2020, **239**, DOI: **10.1016/j.matchemphys.2019.122324**.

16 Z. Guo, N. Liao, M. Zhang and A. Feng, Enhanced gas sensing performance of polyaniline incorporated with graphene: A first-principles study, *Phys. Lett. A*, 2019, **383**, 2751–2754, DOI: **10.1016/j.physleta.2019.03.045**.

17 Y. C. Wong, B. C. Ang, A. S. M. A. Haseeb, A. A. Baharuddin and Y. H. Wong, Review—Conducting Polymers as Chemiresistive Gas Sensing Materials: A Review, *J. Electrochem. Soc.*, 2020, **167**(3), 037503, DOI: **10.1149/2.0032003jes**.

18 M. Reddeppa, *et al.*, UV-light enhanced CO gas sensors based on InGaN nanorods decorated with p-Phenylenediamine-graphene oxide composite, *Sens. Actuators, B*, 2020, **307**(2019), 127649, DOI: **10.1016/j.snb.2019.127649**.

19 T. Aqeel, V. Galstyan and E. Comini, Mesoporous polycrystalline SnO2 framework synthesized by direct soft templating method for highly selective detection of NO2, *Nanotechnology*, 2020, **31**(10), DOI: **10.1088/1361-6528/ab5a1e**.

20 H. Xu, X. Liu, D. Cui, M. Li and M. Jiang, A novel method for improving the performance of ZnO gas sensors, *Sens. Actuators, B*, 2006, **114**, 301–307, DOI: **10.1016/j.snb.2005.05.020**.

21 S. Kumar, *et al.*, Optimization of Pt nanoparticles loading in ZnO for highly selective and stable hydrogen gas sensor at reduced working temperature, *Sens. Actuators, B*, 2023, **375**(2022), 132943, DOI: **10.1016/j.snb.2022.132943**.

22 Y. Jeong, *et al.*, Effects of oxygen gas in the sputtering process of the WO3 sensing layer on NO2 sensing characteristics of the FET-type gas sensor, *Solid-State Electron.*, 2023, **200**(2), 108563, DOI: **10.1016/j.sse.2022.108563**.

23 S. Xue, Z. Huang, M. Yun, D. Liu, Z. Pan and D. Yang, The adsorption characteristics of MoS2–CuO heterojunction to polar gas molecules (CO, NO and NO2): A first–principle study, *Appl. Surf. Sci.*, 2023, **610**(2022), 155564, DOI: **10.1016/j.apsusc.2022.155564**.

24 J. N. Okai Amu-Darko, *et al.*, Metal-organic frameworks-derived In2O3/ZnO porous hollow nanocages for highly sensitive H2S gas sensor, *Chemosphere*, 2023, **314**(2022), 1–9, DOI: **10.1016/j.chemosphere.2022.137670**.

25 M. Kumaresan, M. Venkatachalam, M. Saroja, P. Gowthaman and J. Gobinath, Metal organic frameworks-derived sensing material of TiO2 thin film sensors for detection of NO2 gas, *J. Mater. Sci.: Mater. Electron.*, 2023, **34**(5), DOI: **10.1007/s10854-023-09830-9**.

26 X. Li, *et al.*, Identification of binary gases' mixtures from time-series resistance fluctuations: A sensitivity-controllable SnO2 gas sensor-based approach using 1D-CNN, *Sens. Actuators, A*, 2023, **349**(2022), 114070, DOI: **10.1016/j.sna.2022.114070**.

27 S. J. Jeon, K. H. Oh, Y. Choi, and J. C. Park, "*Highly Dispersed Pt-Incorporated Mesoporous Fe 2 O 3 for Low-Level Sensing of Formaldehyde Gas*, 2023.

28 J. Y. Niu, *et al.*, Mesoporous Co3O4 nanowires decorated with g-C3N4 nanosheets for high performance toluene gas sensors based on p–n heterojunction, *Mater. Chem. Phys.*, 2023, **293**(2022), DOI: **10.1016/j.matchemphys.2022.126980**.

29 V. Balouria, *et al.*, Chemiresistive gas sensing properties of nanocrystalline Co 3O4 thin films, *Sens. Actuators, B*, 2013, **176**, 38–45, DOI: **10.1016/j.snb.2012.08.064**.

30 M. Khan, M. Hussain, S. Crispi, S. Rafique, R. Akram and G. Neri, Effects of Fe2O3 on the magnetic and gas sensing properties of Co3O4 nanoparticles, *Next Mater.*, 2025, **7**(2024), 100338, DOI: **10.1016/j.nxmate.2024.100338**.

31 M. Ullah, *et al.*, Designing of three-dimensional hierarchical Co3O4@g-C3N4 nanostructure with highest surface area for sensitive detection of NO2 gas at room temperature, *Emergent Mater.*, 2024, 1–15, DOI: **10.1007/S42247-024-00826-7/METRICS**.

32 C. Busacca, A. Donato, M. Lo Faro, A. Malara, G. Neri and S. Trocino, CO gas sensing performance of electrospun Co3O4 nanostructures at low operating temperature, *Sens. Actuators, B*, 2020, **303**(2019), 127193, DOI: **10.1016/j.snb.2019.127193**.

33 D. Y. Kim, H. Kang, N. J. Choi, K. H. Park and H. K. Lee, A carbon dioxide gas sensor based on cobalt oxide containing barium carbonate, *Sens. Actuators, B*, 2017, **248**, 987–992, DOI: **10.1016/j.snb.2017.02.160**.

34 G. Joshi, J. K. Rajput and L. P. Purohit, SnO2–Co3O4 pores composites for CO2 gas sensing at low operating temperature, *Microporous Mesoporous Mater.*, 2021, **326**, 111343, DOI: **10.1016/J.MICROMESO.2021.111343**.

35 L. Gómez, V. Galeano, R. Parra, C. R. Michel, C. Paucar and O. Morán, Carbon dioxide gas sensing properties of ordered oxygen deficient perovskite LnBaCo2O5+δ (Ln = La, Eu), *Sens. Actuators, B*, 2015, **221**, 1455–1460, DOI: **10.1016/J.SNB.2015.07.080**.

36 A. Ghosh, C. Zhang, S. Shi and H. Zhang, High temperature CO2 sensing and its cross-sensitivity towards H2 and CO gas using calcium doped ZnO thin film coated langasite SAW sensor, *Sens. Actuators, B*, 2019, **301**, 126958, DOI: **10.1016/J.SNB.2019.126958**.

37 N. M. Abdulmalek and H. A. Jawad, Influence of cobalt doping on structural and optical properties of copper oxide expected as an inorganic hole transport layer for perovskite solar cell, *J. Mater. Sci.: Mater. Electron.*, 2024, **35**(2), 1–13, DOI: **10.1007/S10854-024-11932-X/METRICS**.

38 A. M. Hashem, A. E. Abdel-Ghany, R. S. El-Tawil, A. Mauger and C. M. Julien, Effect of Na Doping on the Electrochemical Performance of Li1.2Ni0.13Co0.13Mn0.54O2 Cathode for Lithium-Ion Batteries, *Sustainable Chem.*, 2022, **3**(2), 131–148, DOI: **10.3390/suschem3020010**.

39 B. Akkinepally, I. N. Reddy, T. J. Ko, K. Yoo and J. Shim, Dopant effect on Li+ ion transport in NASICON-type solid electrolyte: Insights from molecular dynamics simulations and experiments, *Ceram. Int.*, 2022, **48**(9), 12142–12151, DOI: **10.1016/j.ceramint.2022.01.075**.

40 L. N. Ezenwaka, N. S. Umeokwonna and N. L. Okoli, Optical, structural, morphological, and compositional properties of cobalt doped tin oxide (CTO) thin films deposited by modified chemical bath method in alkaline medium, *Ceram. Int.*, 2020, **46**(5), 6318–6325, DOI: **10.1016/J.CERAMINT.2019.11.106**.

41 A. S. Altowyan, *et al.*, Design and Characterization of Zeolite/Serpentine Nanocomposite Photocatalyst for Solar Hydrogen Generation, *Materials*, 2022, **15**(18), DOI: **10.3390/ma15186325**.

42 D. Wang, D. Zhang, X. Chen, H. Zhang, M. Tang and J. Wang, Multifunctional respiration-driven triboelectric nanogenerator for self-powered detection of formaldehyde in exhaled gas and respiratory behavior, *Nano Energy*, 2022, **102**, 107711, DOI: **10.1016/j.nanoen.2022.107711**.

43 S. K. J. Vijitha, K. Mohanraj and R. P. Jebin, Structural, optical, and surface modifications by varying precursor concentrations on spray deposition of In doped Co3O4 thin films for electro chemical application, *Chem. Phys. Impact*, 2023, **6**(2022), 100143, DOI: **10.1016/j.chphi.2022.100143**.

44 A. M. Abdallah and R. Awad, Study of the Structural and Physical Properties of Co3O4 Nanoparticles Synthesized by Co-Precipitation Method, *J. Supercond. Novel Magn.*, 2020, **33**(5), 1395–1404, DOI: **10.1007/s10948-019-05296-1**.

45 L. Sun, H. Li, L. Ren and C. Hu, Synthesis of Co3O4 nanostructures using a solvothermal approach, *Solid State Sci.*, 2009, **11**(1), 108–112, DOI: **10.1016/J.SOLIDSTATESCIENCES.2008.05.013**.

46 Gas Sensing Solutions Ltd, *Pressure Compensation of a Co2 Sensor*, 2021, pp. 1–16.

47 V. Kumar, *et al.*, Environment-sensitive and fast room temperature CO2 gas sensor based on ZnO, NiO and Ni-ZnO nanocomposite materials, *Environ. Funct. Mater.*, 2023, **2**(2), 167–177, DOI: **10.1016/J.EFMAT.2023.12.002**.

48 M. B. Muradov, *et al.*, The effect of Cu doping on structural, optical properties and photocatalytic activity of Co3O4 nanoparticles synthesized by sonochemical method, *Opt. Mater.*, 2023, **142**, 114001, DOI: **10.1016/J.OPTMAT.2023.114001**.

49 M. Shaban, A. Almohammedi, R. Saad and A. M. El Sayed, Design of SnO2:Ni,Ir Nanoparticulate Photoelectrodes for Efficient Photoelectrochemical Water Splitting, *Nanomater*, 2022, **12**(3), 453, DOI: **10.3390/NANO12030453**.

50 M. Shaban, R. Saad and A. M. El Sayed, Influence of chromium and lanthanum incorporation on the optical properties, catalytic activity, and stability of IrOx nanostructured films for hydrogen generation, *Int. J. Hydrogen Energy*, 2023, DOI: **10.1016/j.ijhydene.2022.12.294**.

51 A. S. Altowyan, M. Shaban, K. Abdelkarem and A. M. El Sayed, The Influence of Electrode Thickness on the Structure and Water Splitting Performance of Iridium Oxide Nanostructured Films, *Nanomaterials*, 2022, **12**(19), 3272, DOI: **10.3390/NANO12193272**.

52 F. Gu, C. Li, Y. Hu and L. Zhang, Synthesis and optical characterization of Co3O4 nanocrystals, *J. Cryst. Growth*, 2007, **304**(2), 369–373, DOI: **10.1016/J.JCRYSGRO.2007.03.040**.

53 J. Guo, D. Zhang, T. Li, J. Zhang and L. Yu, Green light-driven acetone gas sensor based on electrospinned CdS nanospheres/Co3O4 nanofibers hybrid for the detection of exhaled diabetes biomarker, *J. Colloid Interface Sci.*, 2022, **606**, 261–271, DOI: **10.1016/j.jcis.2021.08.022**.

54 M. Shkir, *et al.*, Spray pyrolysis developed Nd doped Co3O4 nanostructured thin films and their structural, and opto-nonlinear properties for optoelectronics applications, *Opt. Laser Technol.*, 2022, **150**(2021), 107959, DOI: **10.1016/j.optlastec.2022.107959**.

55 N. M. Shaalan, T. A. Hanafy and M. Rashad, Dual optical properties of NiO-doped PVA nanocomposite films, *Opt. Mater.*, 2021, **119**, 111325, DOI: **10.1016/j.optmat.2021.111325**.

56 S. Mokdad, A. Boukazoula, K. Chouchane, F. Saib, M. Trari and A. Abdi, Electrocatalytic activity of electrodeposited CoOx thin film on low-carbon unalloyed steel substrate toward electrochemical oxygen evolution reaction (OER), *Chem. Pap.*, 2023, **77**(9), 4979–4992, DOI: **10.1007/s11696-023-02837-w**.

57 D. Zhang, L. Yu, D. Wang, Y. Yang, Q. Mi and J. Zhang, Multifunctional Latex/Polytetrafluoroethylene-Based Triboelectric Nanogenerator for Self-Powered Organ-like MXene/Metal-Organic Framework-Derived CuO Nanohybrid Ammonia Sensor, *ACS Nano*, 2021, **15**(2), 2911–2919, DOI: **10.1021/ACSNANO.0C09015**.

58 D. Alburquenque, V. Bracamonte, M. Del Canto, A. Pereira and J. Escrig, Dewetting of Co thin films obtained by atomic layer deposition due to the thermal reduction process, *MRS Commun.*, 2017, **7**(4), 848–853, DOI: **10.1557/mrc.2017.94**.

59 D. Wang, J. Zhou and G. Liu, Effect of Li-doped concentration on the structure, optical and electrical properties of p-type ZnO thin films prepared by sol-gel method, *J. Alloys Compd.*, 2009, **481**, 802–805, DOI: **10.1016/j.jallcom.2009.03.111**.

60 F. Boudjouan, *et al.*, Doping effect investigation of Li-doped nanostructured ZnO thin films prepared by sol-gel process, *J. Mater. Sci.: Mater. Electron.*, 2016, **27**, 8040–8046, DOI: **10.1007/s10854-016-4800-2**.

61 S. N. A. Mustaffa, *et al.*, Sensing mechanism of an optimized room temperature optical hydrogen gas sensor made of zinc oxide thin films, *J. Mater. Res. Technol.*, 2020, **9**(5), 10624–10634, DOI: **10.1016/j.jmrt.2020.07.086**.

62 A. E. Shalan, *et al.*, Cobalt Oxide (CoOx) as an Efficient Hole-Extracting Layer for High-Performance Inverted Planar Perovskite Solar Cells, *ACS Appl. Mater. Interfaces*, 2016, **8**(49), 33592–33600, DOI: **10.1021/acsami.6b10803**.

63 H. Zhang, *et al.*, Ultrastretchable, Self-Healing Conductive Hydrogel-Based Triboelectric Nanogenerators for Human-

Computer Interaction, *ACS Appl. Mater. Interfaces*, 2023, **15**(4), 5128–5138, DOI: **10.1021/ACSAMI.2C17904**.

64 I. A. Zgair, A. H. Omran Alkhayatt, A. A. Muhmood and S. K. Hussain, Investigation of structure, optical and photoluminescence characteristics of Li doped CuO nanostructure thin films synthesized by SILAR method, *Optik*, 2019, **191**, 48–54, DOI: **10.1016/j.ijleo.2019.06.008**.

65 L. Zhang, *et al.*, Fabrication and properties of Li-doped ZnCoO diluted magnetic semiconductor thin films, *Superlattices Microstruct.*, 2011, **50**(3), 261–268, DOI: **10.1016/j.spmi.2011.07.002**.

66 P. Chand, A. Gaur, A. Kumar and U. Kumar Gaur, Structural and optical study of Li doped CuO thin films on Si (1 0 0) substrate deposited by pulsed laser deposition, *Appl. Surf. Sci.*, 2014, **307**, 280–286, DOI: **10.1016/j.apsusc.2014.04.027**.

67 R. F. Fedors, *et al.*, Energy table for EDS analysis, *J. Polym. Sci., Part A: Polym. Chem.*, 1990, **38**(6), 147–154.

68 M. T. V. P. Jayaweera, R. C. L. De Silva, I. R. M. Kottegoda and S. R. D. Rosa, Synthesis, characterization and ethanol vapor sensing performance of SnO2/Graphene composite film, *Sri Lankan J. Phys.*, 2015, **15**, 1, DOI: **10.4038/sljp.v15i0.6345**.

69 A. Maity, A. K. Raychaudhuri and B. Ghosh, High sensitivity NH3 gas sensor with electrical readout made on paper with perovskite halide as sensor material, *Sci. Rep.*, 2019, **9**(1), 1–10, DOI: **10.1038/s41598-019-43961-6**.

70 T. A. Taha, R. Saad, M. Zayed, M. Shaban and A. M. Ahmed, Tuning the surface morphologies of ZnO nanofilms for enhanced sensitivity and selectivity of CO2 gas sensor, *Appl. Phys. A: Mater. Sci. Process.*, 2023, **129**(2), DOI: **10.1007/s00339-023-06387-6**.

71 W. Li, *et al.*, Synergy of Porous Structure and Microstructure in Piezoresistive Material for High-Performance and Flexible Pressure Sensors, *ACS Appl. Mater. Interfaces*, 2021, **13**(16), 19211–19220, DOI: **10.1021/ACSAMI.0C22938/SUPPL_FILE/AM0C22938_SI_001.PDF**.

72 R. Saad, *et al.*, Fabrication of ZnO/CNTs for application in CO2 sensor at room temperature, *Nanomaterials*, 2021, **11**(11), DOI: **10.3390/nano11113087**.

73 K. Abdelkarem, R. Saad, A. M. Ahmed, M. I. Fathy, M. Shaban and H. Hamdy, Efficient room temperature carbon dioxide gas sensor based on barium doped CuO thin films, *J. Mater. Sci.*, 2023, **58**(28), 11568–11584, DOI: **10.1007/S10853-023-08687-X/TABLES/3**.

74 M. Shaban, M. Zayed and H. Hamdy, Nanostructured ZnO thin films for self-cleaning applications, *RSC Adv.*, 2017, 7(2), 617–631, DOI: **10.1039/C6RA24788A**.

75 K. Abdelkarem, R. Saad, A. M. El Sayed, M. I. Fathy, M. Shaban and H. Hamdy, Design of high-sensitivity La-doped ZnO sensors for CO 2 gas detection at room temperature, *Sci. Rep.*, **13**, 18398, DOI: **10.1038/s41598-023-45196-y**.

76 J. Wu, *et al.*, Boosted sensitivity of graphene gas sensor via nanoporous thin film structures, *Sens. Actuators, B*, 2018, **255**, 1805–1813, DOI: **10.1016/j.snb.2017.08.202**.

77 R. Saad, *et al.*, Enhanced CO2 gas sensing at room temperature using Ag-plated Na-doped CuO thin films synthesized by successive ionic layer adsorption and reaction technique, *Surf. Interfaces*, 2024, **44**(2023), 103789, DOI: **10.1016/j.surfin.2023.103789**.

78 V. Balouria, *et al.*, Chemiresistive gas sensing properties of nanocrystalline Co3O4 thin films, *Sens. Actuators, B*, 2013, **176**, 38–45, DOI: **10.1016/J.SNB.2012.08.064**.

79 T. Bhowmick, A. Ghosh, V. Ambardekar, S. Nag and S. B. Majumder, Potential of copper oxide thin film-based sensor probe for carbon dioxide gas monitoring, *J. Mater. Sci.: Mater. Electron.*, 022, **33**(35), 26286–26298, DOI: **10.1007/S10854-022-09312-4/METRICS**.

80 X. Fan, Y. Xu, C. Ma and W. He, In-situ growth of Co3O4 nanoparticles based on electrospray for an acetone gas sensor, *J. Alloys Compd.*, 2021, **854**, 157234, DOI: **10.1016/J.JALLCOM.2020.157234**.

81 A. S. Altowyan, M. Shaban, K. Abdelkarem and A. M. El Sayed, The Impact of Co Doping and Annealing Temperature on the Electrochemical Performance and Structural Characteristics of SnO2 Nanoparticulate Photoanodes, *Materials*, 2022, **15**(19), DOI: **10.3390/ma15196534**.

82 Y. Lu, G. Yang, Y. Shen, H. Yang, and K. Xu, *Multifunctional Flexible Humidity Sensor Systems towards Noncontact Wearable Electronics*, Springer Nature, Singapore, 2022, vol. 14.

83 Z. Ling and C. Leach, The effect of relative humidity on the NO2 sensitivity of a SnO2/WO3 heterojunction gas sensor, *Sens. Actuators, B*, 2004, **102**(1), 102–106, DOI: **10.1016/j.snb.2004.02.017**.

84 J. Fan, *et al.*, Enhanced gas sensing property of Co3O4 matrix nanocomposites with halloysite nanotubes toward triethylamine, *J. Mater. Res. Technol.*, 2023, **23**, 2491–2503, DOI: **10.1016/j.jmrt.2023.01.142**.

85 M. A. Basyooni, M. Shaban and A. M. El Sayed, Enhanced Gas Sensing Properties of Spin-coated Na-doped ZnO Nanostructured Films, *Sci. Rep.*, 2017, **7**, DOI: **10.1038/srep41716**.

86 M. Shaban, K. Abdelkarem and A. M. El Sayed, Structural, optical and gas sensing properties of Cu2O/CuO mixed phase: effect of the number of coated layers and (Cr + S) co-Doping, *Phase Transitions*, 2019, **92**(4), 347–359, DOI: **10.1080/01411594.2019.1581886**.

87 R. Saad, A. M. Ahmed, K. Abdelkarem, M. Zayed and Z. M. Faidey, SILAR-Deposited CuO Nanostructured Films Doped with Zinc and Sodium for SILAR-Deposited CuO Nanostructured Films Doped with Zinc and Sodium for Improved CO 2 Gas Detection, *Nanomaterials*, 2023, **13**(20), 2793, DOI: **10.3390/nano13202793**.

88 T. Thomas, *et al.*, Porous silicon/α-MoO3 nanohybrid based fast and highly sensitive CO2 gas sensors, *Vacuum*, 2021, **184**, 109983, DOI: **10.1016/j.vacuum.2020.109983**.

89 M. Amarnath and K. Gurunathan, Highly selective CO2 gas sensor using stabilized NiO-In2O3 nanospheres coated reduced graphene oxide sensing electrodes at room temperature, *J. Alloys Compd.*, 2021, **857**, 157584, DOI: **10.1016/J.JALLCOM.2020.157584**.

90 J. Herrán, *et al.*, On the structural characterization of BaTiO3-CuO as CO2 sensing material, *Sens. Actuators, B*, 2008, **133**(1), 315–320, DOI: **10.1016/j.snb.2008.02.052**.

91 K.-C. Hsu, T.-H. Fang, Y.-J. Hsiao and C.-A. Chan, Highly response CO2 gas sensor based on Au-La2O3 doped SnO2 nanofibers, *Mater. Lett.*, 2020, **261**, 127144, DOI: **10.1016/j.matlet.2019.127144**.

92 M. Panday, G. K. Upadhyay and L. P. Purohit, Sb incorporated SnO2 nanostructured thin films for CO2 gas sensing and humidity sensing applications, *J. Alloys Compd.*, 2022, **904**, 164053, DOI: **10.1016/j.jallcom.2022.164053**.

93 T. Bhowmick, A. Ghosh, S. Nag and S. B. Majumder, Sensitive and selective CO2 gas sensor based on CuO/ZnO bilayer thin-film architecture, *J. Alloys Compd.*, 2022, **903**, 163871, DOI: **10.1016/J.JALLCOM.2022.163871**.

94 S. T. Navale, *et al.*, Solution-processed rapid synthesis strategy of Co3O4 for the sensitive and selective detection of H2S, *Sens. Actuators, B*, 2017, **245**, 524–532, DOI: **10.1016/j.snb.2017.01.195**.

95 K. Akhmetova, F. Sultanov, A. Mentbayeva, N. Umirov, Z. Bakenov and B. Tatykayev, Advances in multi-element doping of LiFePO4 cathode material for capacity enhancement in Li-ion batteries, *J. Power Sources*, 2024, **624**, 235531, DOI: **10.1016/J.JPOWSOUR.2024.235531**.

96 Z. Cui, H. Wu, K. Yang, X. Wang and Y. Lv, Adsorption of gas molecules on intrinsic and defective MoSi2N4 monolayer: Gas sensing and functionalization, *Sens. Actuators, A*, 2024, **366**, 114954, DOI: **10.1016/J.SNA.2023.114954**.

97 S. Fareed, R. Medwal, J. V. Vas, I. A. Khan, R. S. Rawat and M. A. Rafiq, Tailoring oxygen sensing characteristics of Co3O4 nanostructures through Gd doping, *Ceram. Int.*, 2020, **46**(7), 9498–9506, DOI: **10.1016/J.CERAMINT.2019.12.211**.

98 G. Joshi, J. K. Rajput and L. P. Purohit, SnO2–Co3O4 pores composites for CO2 gas sensing at low operating temperature, *Microporous Mesoporous Mater.*, 2021, **326**, 111343, DOI: **10.1016/j.micromeso.2021.111343**.

99 G. W. C. Kumarage and E. Comini, Low-Dimensional Nanostructures Based on Cobalt Oxide (Co3O4) in Chemical-Gas Sensing, *Chemosens*, 2021, **9**(8), 197, DOI: **10.3390/CHEMOSENSORS9080197**.

100 L. Bigiani, *et al.*, Hydrogen gas sensing performances of p-type Mn3O4 nanosystems: The role of built-in Mn3O4/Ag and Mn3O4/SnO2 junctions, *Nanomaterials*, 2020, **10**(3), 15–19, DOI: **10.3390/nano10030511**.

101 L. Van Duy, *et al.*, Room Temperature Ammonia Gas Sensor Based on p-Type-like V2O5 Nanosheets towards Food Spoilage Monitoring, *Nanomaterials*, 2023, **13**(1), DOI: **10.3390/nano13010146**.

102 D. Puglisi, *et al.*, Review: InfluencFront SensorsProperties on Gas Sensing Characteristics, *Front. Sensors*, 2021, **1**, 657931, DOI: **10.3389/fsens.2021.657931**.

103 A. Samad, D. R. O. Nuñez, G. C. S. Castillo, B. Laquai and U. Vogt, Effect of relative humidity and air temperature on the results obtained from low-cost gas sensors for ambient air quality measurements, *Sensors*, 2020, **20**(18), 1–29, DOI: **10.3390/s20185175**.

104 A. Moumen, G. C. W. Kumarage and E. Comini, P-Type Metal Oxide Semiconductor Thin Films: Synthesis and Chemical Sensor Applications, *Sensors*, 2022, **22**(4), DOI: **10.3390/s22041359**.